

High-Efficiency $(\text{Li}_x\text{Cu}_{1-x})_2\text{ZnSn}(\text{S},\text{Se})_4$ Kesterite Solar Cells with Lithium Alloying

Antonio Cabas-Vidani,* Stefan G. Haass, Christian Andres, Raquel Caballero, Renato Figi, Claudia Schreiner, José A. Márquez, Charles Hages, Thomas Unold, Davide Bleiner, Ayodhya N. Tiwari, and Yaroslav E. Romanyuk

The performance-boosting effect of alkali treatments is well known for chalcogenide thin-film solar cells based on $\text{Cu}(\text{In},\text{Ga})\text{Se}_2$ (CIGS) and $\text{Cu}_2\text{ZnSn}(\text{S},\text{Se})_4$ (CZTSSe–kesterite) absorbers. In contrast to heavier alkali elements, lithium is expected to alloy with the kesterite phase leading to the solid solution $(\text{Li}_x\text{Cu}_{1-x})_2\text{ZnSn}(\text{S},\text{Se})_4$ (LCZTSSe), which offers a way of tuning the semiconductor bandgap by changing the ratio $\text{Li}/(\text{Li}+\text{Cu})$. Here is presented an experimental series of solution-processed LCZTSSe with lithium fraction $\text{Li}/(\text{Li}+\text{Cu})$ ranging from $x = 0$ to 0.12 in the selenized absorber as measured by means of inductively coupled plasma mass spectrometry. The proportional increase in lattice parameter a and bandgap from 1.05 to 1.18 eV confirms the lithium alloying in the kesterite phase. Increase in grain size is observed for x up to 0.07, whereas a higher lithium fraction leads to a porous absorber morphology due to an inhomogeneous distribution of Li-containing compounds in the kesterite layer. An increase of the photoluminescence quantum yield is observed as the Li fraction increases in the absorber layer. A champion device exhibits a remarkable efficiency of 11.6% (12.2% active area) for $x = 0.06$, close to the world record value of 12.6% demonstrating the effectiveness of lithium alloying.

1. Introduction

Kesterite– $\text{Cu}_2\text{ZnSn}(\text{S},\text{Se})_4$ (CZTSSe)–solar cell absorbers are composed of earth abundant and nontoxic elements, which

stimulates active interest to this thin film solar cell technology. The 12.6% efficiency record for kesterite solar cells has not improved since 2014.^[1] Alkali elements for doping or alloying is one of the possible strategies to boost the device performance and the attention has mainly been focused on sodium and heavier alkali elements. Sodium enhances grain size, passivates grain boundaries and increases the net hole carrier concentration in the absorber layer.^[2–4] While heavier alkali elements are detected in the kesterite absorber layer only below atomic percent concentrations and tending to segregate along grain boundaries,^[5–7] lithium can be incorporated at much higher quantities by alloying within the kesterite phase.^[8] First-principle studies^[7] and investigations on stoichiometric Li-alloyed $\text{Cu}_2\text{ZnSnS}_4$ (CZTS)^[8] report that lithium alloys with the kesterite phase by replacing preferentially Cu on 2a sites due to comparable ionic radii of Cu^+

(0.91 Å) and Li^+ (0.90 Å).^[9] Theoretical analysis on chalcopyrite semiconductors shows that the elimination of p – d hybridization lowers the valence band maximum (VBM).^[10] Therefore, bandgap widening is expected when substituting Cu for an element not belonging to the d-block of the periodic Table like Li. Ultraviolet photoelectron spectroscopy (UPS) measurements on LCZTSSe solar cells further confirm that Li incorporation is shifting prevalently the position of the VBM.^[11] Thus, Li-alloying offers a new way of tailoring the bandgap similar to the previously reported exchange of Se for S^[12,13] or Ge for Sn.^[14–16]


A survey of recent studies of Li-containing CZTSSe devices as shown in Table 1, indicates contrasting and ambiguous results. First, lithium losses of up to 99% from the initial (nominal) concentration to the measured lithium amount in the absorber have been reported, which complicates the quantitative evaluation of lithium influence.^[17] The losses are explained by Yang et al.^[17] through an exchange of Li with Na diffusing from the soda-lime glass (SLG) substrate to the surface of the absorber. The reported increase in grain size is then attributed to Na, although the transport of Na through the gas-phase is not taken into account.^[2,18] Xin et al.^[19] confirms the Li–Na exchange by means of X-ray photoelectron spectroscopy measurements on samples with SLG substrate, but claims no significant morphology change, contrary to Yang et al.^[17]

A. Cabas-Vidani, Dr. S. G. Haass, C. Andres, Prof. A. N. Tiwari, Dr. Y. E. Romanyuk
Laboratory for Thin Films and Photovoltaics
Empa-Swiss Federal Laboratories for Materials Science and Technology
Ueberlandstrasse 129, 8600 Dübendorf, Switzerland
E-mail: antonio.cabasvidani@empa.ch

Dr. R. Caballero
Departamento de Física Aplicada
Universidad Autónoma de Madrid
C/ Francisco Tomás y Valiente 7, 28049 Madrid, Spain

R. Figi, C. Schreiner, Dr. D. Bleiner
Laboratory for Advanced Analytical Technologies
Empa-Swiss Federal Laboratories for Materials Science and Technology
Ueberlandstrasse 129, 8600 Dübendorf, Switzerland

Dr. J. A. Márquez, Dr. C. Hages, Dr. T. Unold
Dept. Structure and Dynamics of Energy Materials
Helmholtz-Zentrum für Materialien und Energie GmbH
Hahn-Meitner-Platz 1, D-14109 Berlin, Germany

 The ORCID identification number(s) for the author(s) of this article can be found under <https://doi.org/10.1002/aenm.201801191>.

DOI: 10.1002/aenm.201801191

Table 1. Comparison of results from recent publications on LCZTSSe-based solar cells. All absorbers were prepared by a solution-based approach except when noted otherwise.

Reference	Maximum nominal $x^a)$	Maximum measured $x^b)$	Maximum solar cell η , relative improvement ^{c)}
Yang et al. ^[11]	0.32	0.22	6.0%, 2.1
Yang et al. ^[17]	0.32	3.4×10^{-4}	6.7%, 1.2
Xin et al. ^[19]	0.022	3.9×10^{-5}	10.5%, 1.2
Haass et al. ^[20]	0.15	0.034	11.5%, 2.7
Altamura et al. ^[22]	0.4M ^{d)}	Not present	6.0%, 1.5
Hsie et al. ^[45]	0.16	Not present	5.2%, 1.3
Mule et al. ^[21]	Not present	Not present	6.6%, 1.3

^{a)}Ratio was calculated based on concentration values reported in cited papers; ^{b)}Measured with ICP-MS or ICP-OES; ^{c)}Relative improvement ratio: highest efficiency with Li over declared baseline efficiency without Li; ^{d)}Electrostatic spray-assisted vapor deposition.

Second, no correlation appears among the shown studies between measured lithium concentration in the absorber layer and the relative improvement over the baseline process of the solar cells, possibly due to the lack of alkali-barrier layer on SLG substrate (except for SiO_x barrier for Haass et al.^[20] and Yang et al.^[11] who used quartz substrate), hence the difficulty to discriminate between the Li and Na effect. Finally, ranking of alkali elements by Mule et al.^[21] Altamura et al.^[22] and Haass et al.^[20] is not unanimous in identifying the most performing one. These inconsistencies lead to the question: Can high amounts of lithium be incorporated into the kesterite phase, and if yes, what is the impact on solar cell device performance?

The present study aims to unveil the effects of lithium incorporation into the kesterite absorber layer on morphology and device performance and explains the Li-loss phenomenon for a wide range of lithium concentrations. The approach of spin-coating dimethylsulfoxide (DMSO) precursor solutions with subsequent selenization is used to obtain (Li_xCu_{1-x})₂ZnSn(S,Se)₄ (LCZTSSe) absorber layers. Lithium is added directly in various concentrations as lithium chloride

Table 2. Concentration of LiCl in $\times 10^{-3}$ M and calculated nominal x inside the precursor solution compared to the measured x in the selenized LCZTSSe absorber using ICP-MS.

LiCl in precursor solution [$\times 10^{-3}$ M]	Nominal x in precursor solution	Measured x in selenized absorber
10	0.02	0.004
100	0.15	0.034
200	0.26	0.06
300	0.35	0.073
500	0.47	0.1
1000	0.64	0.12

(LiCl) to the precursor solution and the ratio Li/(Li+Cu) is presented as x throughout the manuscript and refers to the measured Li fraction in the selenized absorber layer if not stated otherwise. **Table 2** shows the full set of investigated samples with various nominal lithium concentrations in the precursor solutions. The actual concentrations were measured with inductively coupled plasma mass spectrometry (ICP-MS) in the selenized absorber layer.

2. Results and Discussion

The scanning electron microscope (SEM) cross sections of LCZTSSe devices for lithium fraction ranging from $x = 0$ –0.12 are shown in **Figure 1**. Starting from a bilayer structure with a small-grain bottom layer and bigger grains in the upper crust for the Li-free sample ($x = 0$), the absorber layer exhibits an increasingly homogeneous and compact morphology up to $x = 0.07$. The improvement in grain growth can be explained with the fluxing effect of the Li₂Se phase that is liquid at the holding temperature of 300 °C during the first annealing stage,^[23] similarly to what was reported for the fluxing Na₂Se_x phases.^[4] For $x > 0.07$ the absorber porosity increases and the grain size decreases. As visible from the SEM top view (Figure S1, Supporting Information), the porosity coincides with the

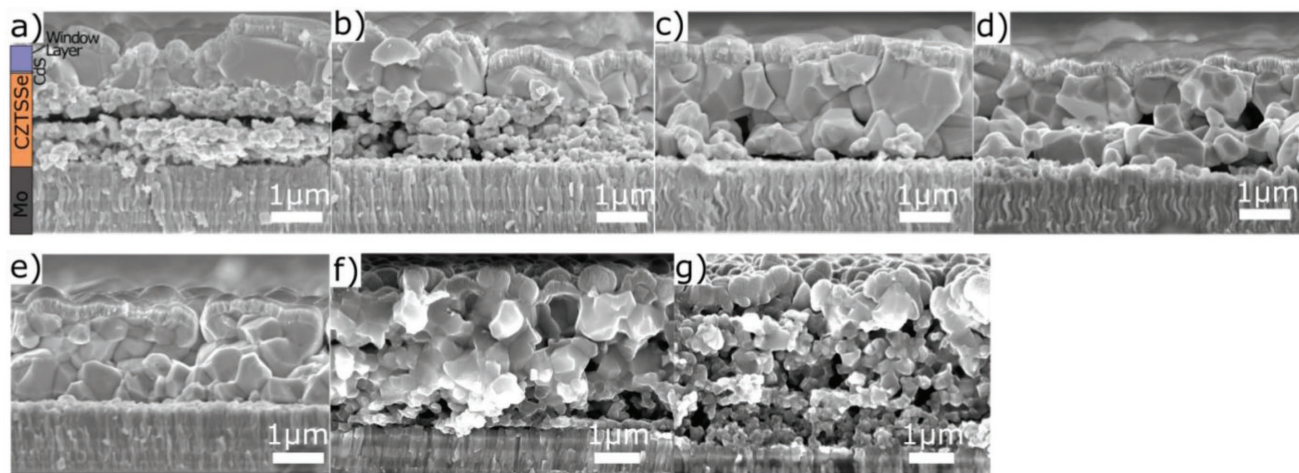


Figure 1. SEM cross-section images of completed solar cell devices with increasing measured x : a) 0, b) 0.004, c) 0.03, d) 0.06, e) 0.07, f) 0.10, and g) 0.12.

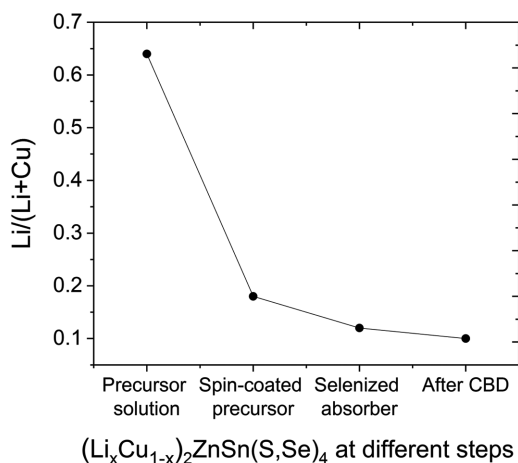


Figure 2. Li content as measured by ICP-MS at different steps of the device processing. The standard deviation of the Li and Cu content is <2% relative for three independent measurements using ICP-MS.

dendritic-shaped features formed during the drying step of the spin-coating process. The maximum LiCl amount used in the precursor solutions is below the solubility limit in DMSO,^[24] but unlike the other metal-chloride salts used in the solution, LiCl does not form sulfide complexes with thiourea (TU).^[25] This might cause the inhomogeneous distribution of Li compounds and, hence the formation of dendritic features. A demonstration experiment described in Figure S2 in the Supporting Information supports this idea.

From Table 2 an average loss of $\approx 80\%$ of the nominal x fraction in the solution compared to the measured x fraction inside the selenized absorber layer can be deduced. To understand the origin of the lithium loss, ICP-MS measurements of the precursor layer, the selenized absorber layer and the selenized absorber layer after CdS deposition were performed on a set of samples processed from a solution with nominal fraction $x = 0.64$ (Figure 2). About 70% of the total loss already occurs during the spin-coating step. Evaporation of lithium compounds is ruled out because their melting point is above 400°C .^[26] The activity coefficient of LiCl in DMSO is negative; hence, the solution shows a negative deviation from

Raoult's law, which implies a decreased volatility from ideal behavior.^[27] The Li loss can be explained by a re-dissolution of soluble Li salts in DMSO during subsequent spin-coating cycles as described in Figure S3 in the Supporting Information.

The complete chemical compositions of all LCZTSse selenized absorber layers as determined by ICP-MS are given in Table S1 in the Supporting Information. As the amount of Li increases, there is no change in Cu/Zn and the variation in Cu/Sn is not related to Li fraction. The ratios $(\text{Cu}+\text{Li})/(\text{Zn}+\text{Sn})$ and Zn/Sn are still in the (Cu+Li)-poor and Zn-rich region as compared to stoichiometric $(\text{Li}_x\text{Cu}_{1-x})_2\text{ZnSnSe}_4$; hence, the phase is rich in Cu vacancies.^[28] A first-principle study showed small substitution and migration energies for Li^+ in stoichiometric CZTSe absorbers^[7] and the presence of Cu vacancies further decreases the migration energy of Li^+ . Thus, Li^+ ions are expected to migrate into the vacancies, instead of substituting Cu.

Figure 3a shows elemental depth profiles obtained from time-of-flight secondary ion mass spectrometry (TOF-SIMS) for samples with $x = 0.03, 0.10$, and 0.12 . The TCO was etched away by dipping the sample in 5% acetic acid solution for 1 min (no influence from the etching on the depth profiles was observed for similar samples, not presented here). Lithium was found homogeneously distributed in the whole absorber layer, though the measurement cannot discriminate if it is segregated at the grain boundaries or uniformly alloyed within the grains. The SiO_x barrier layer reduces the diffusion of impurities from the SLG substrate through the Mo back contact into the absorber layer and sodium exhibits a flat depth profile throughout the absorber as well (Figure 3b). Therefore, the previously reported Li-Na exchange is not observed in our case.^[17]

Figure 4a shows X-ray diffraction (XRD) patterns ($10^\circ < 2\theta < 80^\circ$) for samples with a lithium fraction up to $x = 0.07$. Bragg reflexes at 17.39° , 27.15° , and 45.17° confirm unambiguously the CZTSse phase.^[29] No secondary phases can be identified, although the presence of $\text{Zn}(\text{S,Se})$ and $\text{Cu}_2\text{Sn}(\text{S,Se})_3$ impurity phases cannot be excluded since their Bragg reflexes coincide with those of CZTSse and therefore cannot be distinguished by XRD.^[30] The magnified 112 Bragg peak is shown in Figure 4b where a shift toward smaller angles with increasing lithium fraction is observed. While Li^+ and Cu^+ ionic radii are comparable,^[9] there is a difference in the

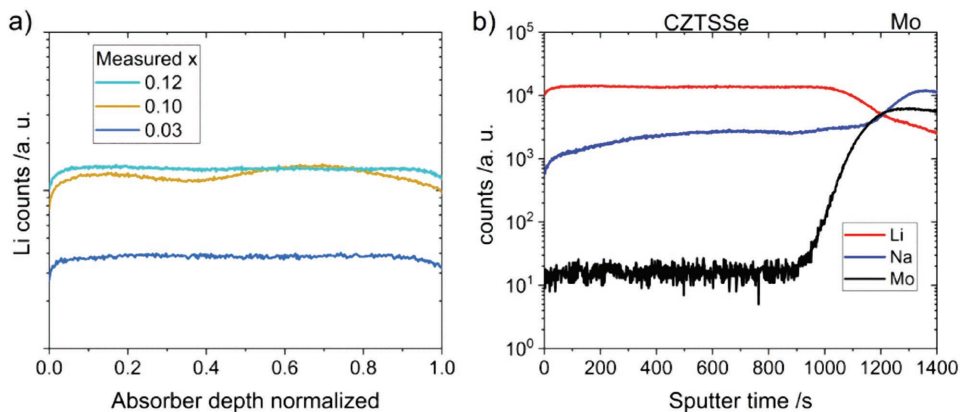


Figure 3. a) Comparison of TOF-SIMS depth profiles of lithium for devices with measured $x = 0.03, 0.10$, and 0.12 . b) TOF-SIMS depth profile of a solar cell with $x = 0.12$ after etching the TCO layer.

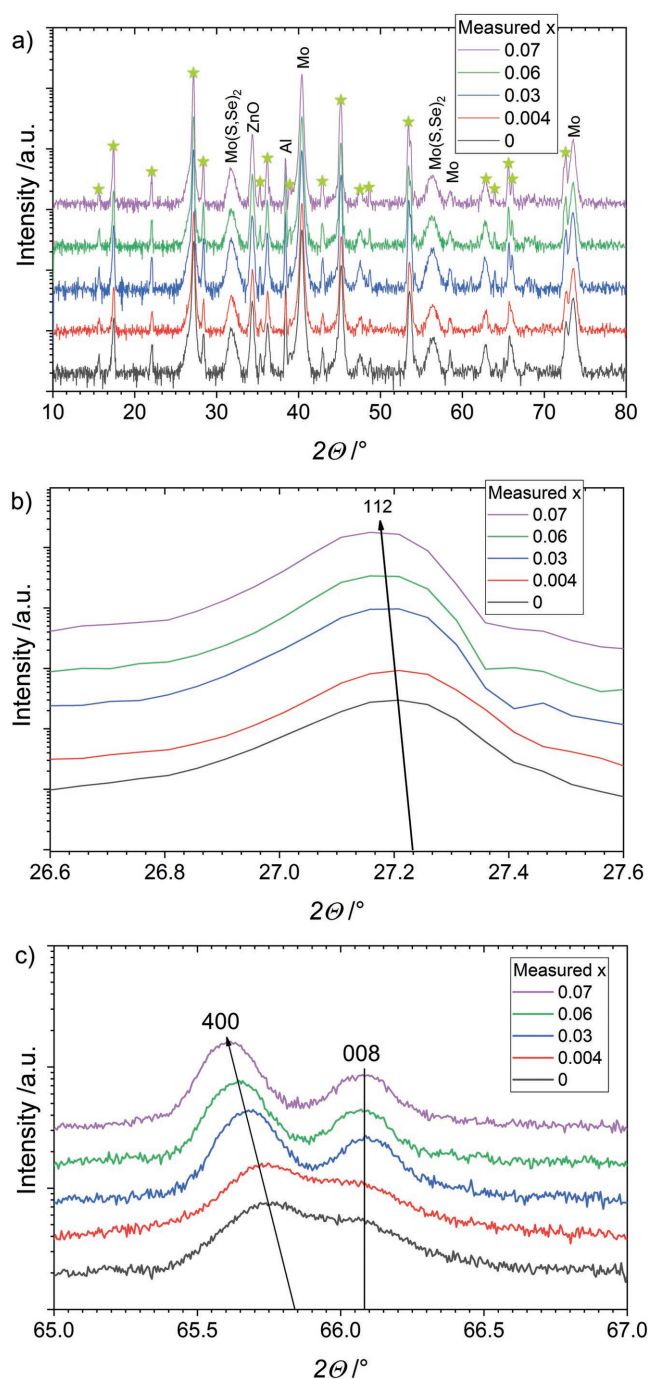


Figure 4. XRD pattern of samples with $x = 0$ – 0.07 . a) Full XRD pattern for ($10^\circ < 2\theta < 80^\circ$). CZTSSe Bragg reflexes are marked with a star*. b) Zoomed 112 Bragg peak from the full XRD pattern. c) High-resolution XRD pattern ($65^\circ < 2\theta < 67^\circ$) after stripping the $K\alpha_2$ signal.

bond valence parameter with 2.09 \AA for Li–Se and 2.02 \AA for Cu–Se. This results in longer bonding distances for Li–Se (same for sulfides)^[31] and therefore triggers the shift of XRD Bragg reflexes toward lower diffraction angles. A thorough study on lithium-alloyed CZTS by Lafond et al.^[8] reports that Li occupies preferentially 2a sites of the lattice unit, thereby increasing the unit cell volume and influencing predominantly the lattice

parameter a . The present samples have a Cu-poor and Zn-rich composition; hence, Cu-vacancies are energetically favorable defects^[32,33] which are preferentially located at 2a sites.^[34] In Figure 4c, XRD scans of the 400–008 Bragg peaks reveal a shift of the 400 Bragg reflex toward lower angles. This shift correlates with an increase in Li fraction, whereas the 008 Bragg reflex remains unaffected, indicating that only the lattice parameter a is increasing. It was also reported previously that a change in c parameter indicates a change in the order/disorder of the Cu/Zn sublattice.^[35,36] Lafond et al.^[8] report an alteration of the disordering process only for $x > 0.5$ and no change in the c parameter is observed in our series, but the overlap of different kinetics due to change in composition, shift of the Bragg peaks due to Li incorporation and change in ordering could sum up to no peak shift. Therefore, additional experiments would be required to verify this possibility.

Following the successful alloying of lithium within the kesterite phase a detailed investigation on its effects on the PV performance is conducted. **Figure 5a** exhibits external quantum efficiency (EQE) spectra for solar cells with lithium fraction ranging from $x = 0$ – 0.12 . The blueshift of the long-wavelength EQE edge correlates with the bandgap increase that is proportional to the lithium fraction. This trend is analogous to what Lafond et al. reported^[8] and it is expected as the bandgap of $\text{Li}_2\text{ZnSnSe}_4$ phase is of 2.0 eV .^[37]

The decreasing parasitic absorption of the CdS layer for the samples with a Li fraction of up to $x = 0.07$ (Figure 5b), suggests that the CdS layer becomes thinner for higher lithium fractions. The reasons for this observation remain unclear. Scattered results in CdS wavelength region for films with $x > 0.07$ are caused presumably by film porosity and increased roughness.

The apparent carrier concentration measured by capacitance–voltage (CV) at room-temperature (**Figure 6**) reveals an increase from $3 \times 10^{15} \text{ cm}^{-3}$ for the sample without lithium up to $5 \times 10^{16} \text{ cm}^{-3}$ for the sample with $x = 0.07$. From the increase in the apparent carrier concentration consequently follows a reduction in the space charge region width down to 60 nm which is also in agreement with the reduced collection in the long-wavelength region in Figure 5. The same observation applies to CZTSSe absorbers when increasing the Cu fraction from a Cu poor composition,^[20] which further supports the assumption that Li is located at Cu vacancies in the lattice. Similarly for Na doped CZTS and $\text{Cu}(\text{In,Ga})\text{Se}_2$ (CIGS) absorbers,^[46,47] it is believed that the formation of Zn_{Cu} donor defects is inhibited by the alkali metal resulting in an increase of hole concentration and decrease of compensation.

Current density–voltage (J – V) parameters (**Figure 7**) are correlated with the absorber morphology evolution. For devices with lithium fraction $x = 0.03$, 0.06 , and 0.07 , the conversion efficiencies consistently and reproducibly exceed 11%. Absorber porosity and inhomogeneous distribution of lithium-containing compounds for devices with $x = 0.10$ and 0.12 affect primarily fill-factor (FF) and short-circuit current density (J_{sc}), causing the efficiency to drop below 8%.

To assess the stability of the Li-containing devices, non-encapsulated solar cells with x from 0 to 0.07 were measured again after 12 months of storage in a dark dry box. The devices with $x = 0.06$ and 0.07 even improved in efficiency, while the

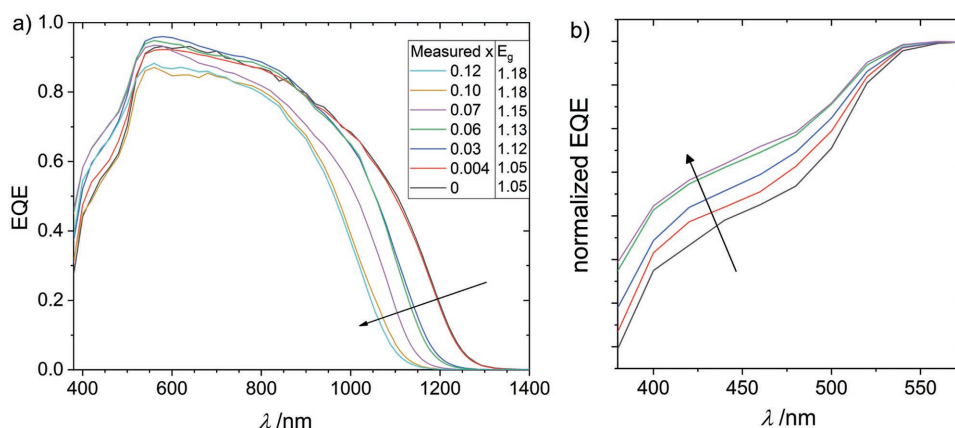


Figure 5. a) EQE spectra for samples with $x = 0$ –0.12. b) Normalized EQE spectra for samples with $x = 0$ –0.07. It indicates a decreased parasitic absorption from CdS layer with higher Li fractions.

others worsened (Figure S4, Supporting Information). Additionally, a sample with $x = 0.06$ without antireflective coating (ARC) was heated on a hotplate in air at 60 °C for 3 days. After the first hour of postannealing, the performance steadily decreased mainly due to a worsening of the FF and J_{sc} parameters, which can be explained through a worsening of interfaces quality rather than instability of the alloy. Interestingly, after 3 days of postannealing the V_{oc} increased due to a bandgap widening from 1.10 to 1.13 eV (Figure S5, Supporting Information).

The solar cells show an increase of the external photoluminescence (PL) quantum yield as x increases in the absorber (Figure 8). The logarithm of the PL quantum yield is inversely proportional to the V_{oc} loss in the device.^[38–40] The observed increase in the PL quantum yield with lithium fraction x indicates a decrease of the amount of non-radiative recombination and therefore a decrease of the quasi-Fermi level splitting loss with respect to the open circuit voltage in the Shockley–Queisser limit (V_{oc-SQ}). This supports that the enhancement on the performance of the solar cells with increased Li fraction is mainly driven by improvements in V_{oc} . Under low injection conditions, the internal PL yield is equal to the product of the minority carrier lifetime (τ_n), the majority charge carrier concentration (p_0) and the material specific radiative recombination coefficient (B).^[41–43] In order to evaluate the origin of the improvements in V_{oc} , we have estimated the minority carrier lifetime from

the PL quantum yield with the procedure described in previous studies.^[41,42] Under the reasonable assumption that B does not change significantly with x and that the apparent carrier concentration derived from C – V approximates p_0 , we conclude that the observed increase in PL quantum yield (and quasi-Fermi level splitting) is mainly driven by the increase of p_0 and not to a significant increase in τ_n (see Table S2 in the Supporting Information for further information).

Finally, Figure 9 demonstrates dark and illuminated J – V curves from the champion device with $x = 0.06$ and a bandgap of 1.13 eV. The V_{oc} loss is the lowest of the investigated series and amounts to 0.35 V when expressed as V_{oc-SQ} -deficit = $V_{oc-SQ} - V_{oc}$ with respect to the Shockley–Queisser limit ($V_{oc-SQ} = 0.932 \times E_g - 0.167$),^[39] and to 0.60 V if expressed as $V_{oc-deficit} = E_g - V_{oc}$. The power conversion efficiency is 11.6% that is determined for a designated illumination area of 0.285 ± 0.003 cm² including front contact metal grid (active area efficiency excluding metal grid shading is 12.2%).

3. Conclusion

In the present study, we accomplished to obtain a lithium alloyed $(Li_xCu_{1-x})_2ZnSn(S,Se)_4$ kesterite absorber layer with x of up to 0.12. A combination of SIMS, ICP-MS, XRD, and

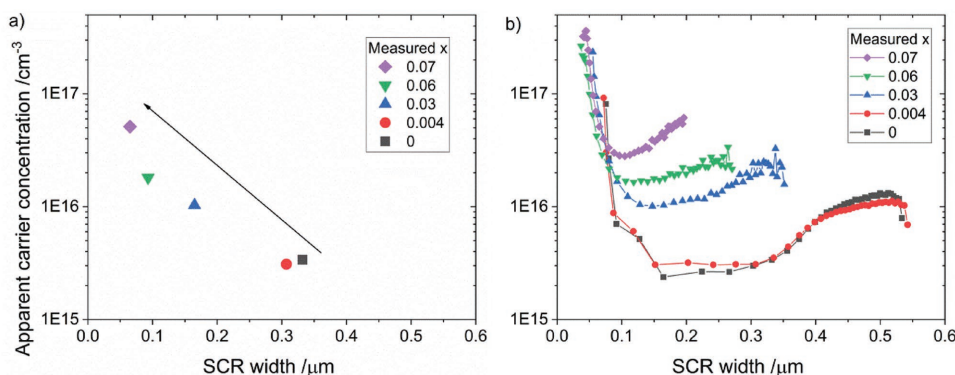


Figure 6. Apparent carrier concentration determined by room-temperature C – V measurements at a) 0 V and in the range of b) -1.5 to 0.5 V.

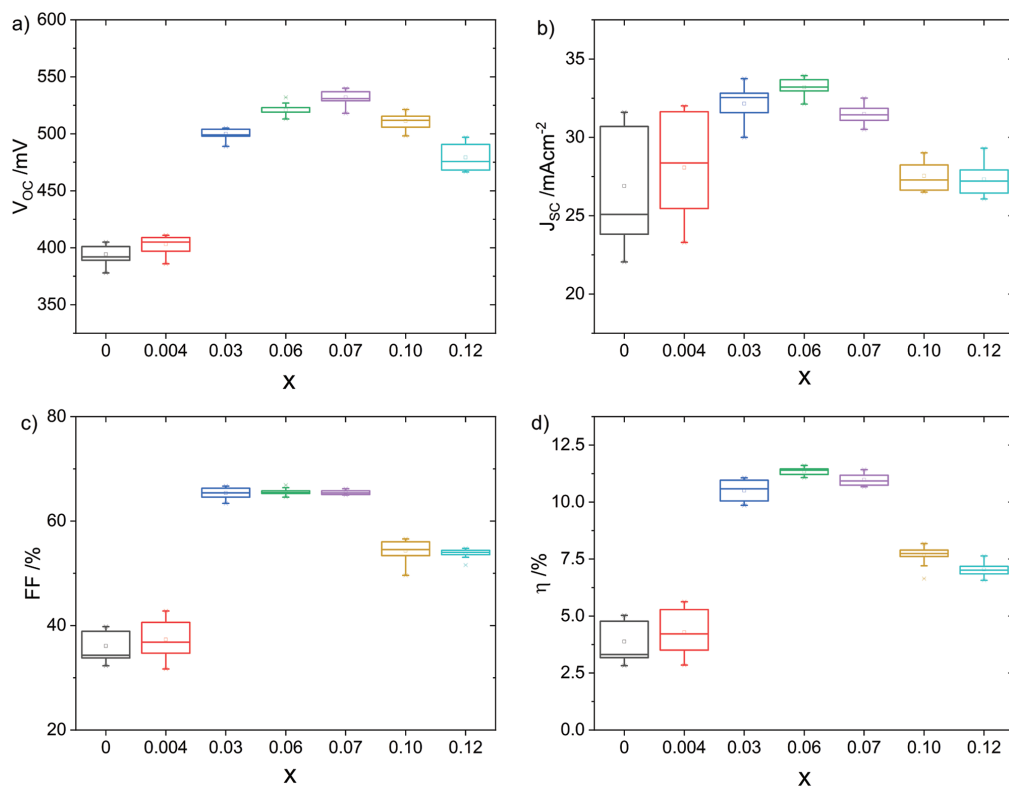


Figure 7. Photovoltaic parameters of $(\text{Li}_x\text{Cu}_{1-x})_2\text{ZnSn}(\text{S,Se})_4$ -based thin-film solar cells as a function of measured Li fraction x . a) Open-circuit voltage (V_{oc}), b) short circuit current (J_{sc}), c) fill factor (FF), and d) efficiency (η). Solar cells for $0 < x < 0.07$ were measured with ARC, and for $x > 0.07$ without ARC. Measurements represent nine cells with an area of 0.3 ± 0.02 cm².

EQE measurements of the absorber layer confirm that lithium is incorporated and alloyed within the kesterite phase. The Li loss reported in earlier studies is explained by the re-dissolution of lithium compounds during the spin-coating and drying step. The apparent carrier concentration increases up to 5×10^{16} cm⁻³ when increasing Li to $x = 0.07$. The high lithium fraction helps to boost the performance of kesterite solar cells as compared to nominally undoped absorbers. This is further confirmed by quantitative PL measurements where an increase of the quantum yield is observed as the Li increases in the absorber layer. The increase in Li fraction, however, does not increase the minority carrier lifetime in

the absorber layers. The decrease of V_{oc-SQ} -deficit observed is a consequence of an increased majority carrier concentration upon Li incorporation. The champion device exhibits an efficiency of 11.6% (12.2% active area) for $x = 0.06$. The beneficial effects of lithium alloying in kesterites indicate that it is worth investigating even higher concentrations of lithium, which requires finding an alternative solution chemistry to reduce the Li loss, as well as exploring the effect of lithium alloying on related CIGS absorbers.

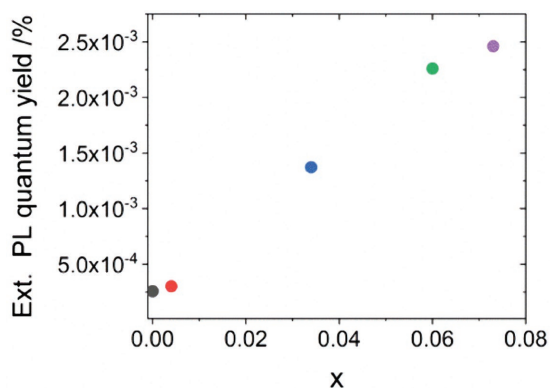


Figure 8. External PL quantum yield as a function of Li fraction x .

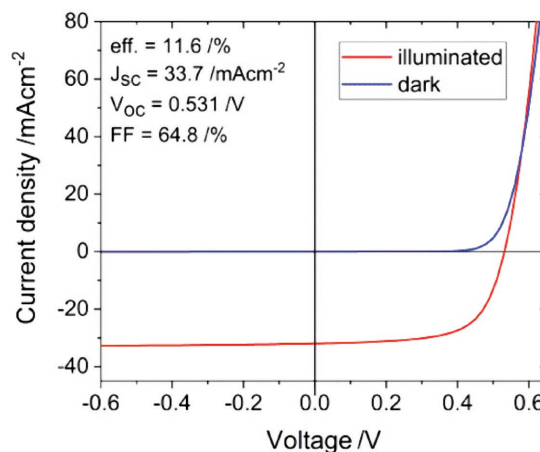


Figure 9. Dark and illuminated J - V measurements for the champion device with $x = 0.06$.

4. Experimental Section

The precursor solution consisted of thiourea (99%+, Sigma-Aldrich), tin chloride dihydrate ($\text{SnCl}_2 \cdot 2\text{H}_2\text{O}$, 98%, Sigma-Aldrich), zinc chloride (ZnCl_2 , 99.99%, Alfa Aesar), and copper chloride dihydrate ($\text{CuCl}_2 \cdot 2\text{H}_2\text{O}$, $\geq 99.99\%$, Sigma-Aldrich), dissolved in dimethyl sulfoxide (DMSO, 99.9%, Alfa Aesar). A 200–300 nm thick SiO_x alkali diffusion barrier layer was sputtered onto a 1 mm thick SLG with a subsequent deposition of 1 μm of molybdenum. The precursor solution was spin coated onto the Mo layer and dried on a hotplate at 320 °C in air. The spin-coating and drying steps were repeated 12 times in order to obtain the desired precursor film thickness of 1.5 μm . All samples were annealed in a rapid thermal processing furnace (RTP Annealsys AS ONE 150) inside a closed graphite box with selenium pellets (800 mg). The temperature gradient employed for annealing was the three-stage process with holding at 300, 500, and 550 °C.^[44] After selenization the absorbers were immersed for 30 s in a 10 wt% KCN solution in order to clean the surface from contaminations and oxides. A 50–70 nm thick CdS buffer layer was deposited by chemical bath deposition, and 70/250 nm i-ZnO/Al:ZnO bilayer was sputtered. A Ni/Al top grid and an antireflection coating of MgF_2 were deposited by e-beam evaporation. Individual solar cells were mechanically scribed to an area of $0.30 \pm 0.02 \text{ cm}^2$.

For ICP-MS analysis, the kesterite absorber material was detached from the thin-film solar cell at the Mo/CZTSSe interface, directly transferred into 50 mL trace metal-free polyethylene tubes, rinsed by HNO_3 1 M suprapure 24 h, and fully dissolved in a mixture of 2.5 mL H_2O_2 30% MERCK suprapure, 4 mL HNO_3 67% MERCK ultrapure, and 2.5 mL HCl 32% MERCK ultrapure. After filling to 25 mL with 18 M Ω cm deionized water, the sample was diluted 1:10 with 18 M Ω cm deionized water for analysis. Metal quantity determination was performed on an Agilent 8800 triple quadrupole ICP-MS with different reaction modes such as He and O_2 and external calibration using certified metal standards (1000 $\mu\text{g mL}^{-1}$, Alfa Aesar Specpure). For quality assurance, analysis of reference materials and spiking experiments were performed, with recoveries between 90% and 110%. SEM and EDX measurements were done on a Hitachi S-4800 electron microscope, XRD patterns for thin films were recorded in $2\theta/\theta$ scan mode using a Bruker D8 diffractometer with Cu K α radiation ($\lambda = 1.5418 \text{ \AA}$, beam voltage: 40 kV, beam current: 40 mA, calibrated using Si100 and Si111 single crystals), a step size of 0.05° , and a scan rate of 0.5 s step^{-1} for the full pattern and a step size of 0.005° and a scan rate of 2 s step^{-1} for the high resolution pattern. XRD patterns for powders were recorded in $2\theta/\theta$ scan mode using a X'Pert PRO Panalytical with Cu K α radiation ($\lambda = 1.5406 \text{ \AA}$, beam voltage: 45 kV, beam current: 40 mA) a step size of 0.016° , and a scan rate of 0.5 s step^{-1} from 10 to 80° (2θ) and fitted with the Match! software.

The J - V characterization was performed under standard test conditions (100 mW cm^{-2} , 25 °C, AM1.5G solar spectrum) using a solar simulator calibrated with a certified Si diode. The EQE spectra were recorded using a chopped white light source (900 W halogen lamp) with a LOT MSH-300 monochromator, which was calibrated with certified Si and Ge diodes. The illuminated area on the sample was 0.1 cm^2 including grid lines. The intensity calibrated PL data was acquired with a custom setup described elsewhere.^[42] The excitation was carried out with 660 nm lasers coupled to homogenizer units. The excitation intensity was equivalent to 2 suns ($\approx 6 \times 10^{21} \text{ photons m}^{-2} \text{ s}^{-1}$). Room-temperature CV measurements were carried out with a LCR meter from Agilent (E4990A) with an AC voltage of 30 mV at 25 °C. Depth profile measurements were done with a TOF-SIMS system from ION-TOF using O^{+2} primary ions with 2 keV of ion energy, a current of 400 nA, and a raster size of $300 \times 300 \mu\text{m}^2$. An area of $100 \times 100 \mu\text{m}^2$ in the case of depth profiles was analyzed using Bi^{+} ions with 25 keV of ion energy. The lithium dependence study ranged from nominal lithium concentration inside the precursor solution of $\text{Li}/(\text{Li}+\text{Cu}) = 0$ –0.64 and it was carried out in two separate series: the first one with nominal $\text{Li}/(\text{Li}+\text{Cu})$ from 0 to 0.35 and the second one followed for $\text{Li}/(\text{Li}+\text{Cu}) = 0.47$ and 0.64. XRD and CV measurements were performed on the first series only.

Supporting Information

Supporting Information is available from the Wiley Online Library or from the author.

Acknowledgements

A.C.-V. and S.G.H. contributed equally to this work. This research was supported by the Horizon2020 program under the project STARCELL (H2020-NMBP-03-2016-720907). R.C. also acknowledges financial support from Spanish Ministry of Education, Culture, and Sport within the José Castillejo program (CAS 15/00070) and MINECO within the Ramón y Cajal program (RYC-2011-08521). The authors would also like to thank the laboratory for Transport at Nanoscale Interfaces and the whole team of the laboratory for Thin Films and Photovoltaics.

Conflict of Interest

The authors declare no conflict of interest.

Keywords

alkali doping, CZTSe, kesterite, lithium, thin film solar cells

Received: April 19, 2018

Revised: August 4, 2018

Published online:

- [1] W. Wang, M. T. Winkler, O. Gunawan, T. Gokmen, T. K. Todorov, Y. Zhu, D. B. Mitzi, *Adv. Energy Mater.* **2014**, *4*, 1.
- [2] T. Abzieher, T. Schnabel, M. Hetterich, M. Powalla, E. Ahlswede, *Phys. Status Solidi A* **2016**, *213*, 1039.
- [3] T. Gershon, B. Shin, N. Bojarczuk, M. Hopstaken, D. B. Mitzi, S. Guha, *Adv. Energy Mater.* **2015**, *5*, 1.
- [4] C. M. Sutter-Fella, J. a. Stükelberger, H. Hagendorfer, F. La Mattina, L. Kranz, S. Nishiwaki, A. R. Uhl, Y. E. Romanyuk, A. N. Tiwari, *Chem. Mater.* **2014**, *26*, 1420.
- [5] T. Schwarz, O. Cojocaru-Mirédin, P. Choi, M. Mousel, a. Redinger, S. Siebentritt, D. Raabe, *J. Appl. Phys.* **2015**, *118*, 095302.
- [6] P. Reinhard, B. Bissig, F. Pianezzi, E. Avancini, H. Hagendorfer, D. Keller, P. Fuchs, M. Döbeli, C. Vigo, P. Crivelli, S. Nishiwaki, S. Buecheler, A. N. Tiwari, *Chem. Mater.* **2015**, *27*, 5755.
- [7] T. Maeda, A. Kawabata, T. Wada, *Phys. Status Solidi C* **2015**, *12*, 631.
- [8] A. Lafond, C. Guillot-Deudon, J. Vidal, M. Paris, C. La, S. Jobic, *Inorg. Chem.* **2017**, *56*, 2712.
- [9] R. D. Shannon, *Acta Crystallogr., Sect. A* **1976**, *32*, 751.
- [10] J. E. Jaffe, A. Zunger, *Phys. Rev. B* **1983**, *27*, 5176.
- [11] Y. Yang, X. Kang, L. Huang, D. Pan, *ACS Appl. Mater. Interfaces* **2016**, *8*, 5308.
- [12] S. Chen, A. Walsh, J.-H. Yang, X. G. Gong, L. Sun, P.-X. Yang, J.-H. Chu, S.-H. Wei, *Phys. Rev. B* **2011**, *83*, 125201.
- [13] O. Gunawan, T. Gokmen, C. W. Warren, J. D. Cohen, T. K. Todorov, D. A. R. Barkhouse, S. Bag, J. Tang, B. Shin, D. B. Mitzi, *Appl. Phys. Lett.* **2012**, *100*, 253905.
- [14] S. Bag, O. Gunawan, T. Gokmen, Y. Zhu, D. B. Mitzi, *Chem. Mater.* **2012**, *24*, 4588.
- [15] R. Caballero, I. Victorov, R. Serna, J. M. Cano-Torres, C. Maffiotte, E. Garcia-Llamas, J. M. Merino, M. Valakh, I. Bodnar, M. León, *Acta Mater.* **2014**, *79*, 181.

- [16] J. Márquez, H. Stange, C. J. Hages, N. Schaefer, S. Levchenko, S. Giraldo, E. Saucedo, K. Schwarzburg, D. Abou-Ras, A. Redinger, M. Klaus, C. Genzel, T. Unold, R. Mainz, *Chem. Mater.* **2017**, 29, 9399.
- [17] Y. Yang, L. Huang, D. Pan, *ACS* **2017**, 9, 23878.
- [18] C. M. Sutter-Fella, *Ph.D. Thesis*, ETH Zürich, Zurich, Germany **2014**.
- [19] H. Xin, S. M. Vorpahl, A. D. Collord, I. L. Braly, A. R. Uhl, B. W. Krueger, D. S. Ginger, H. W. Hillhouse, *Phys. Chem. Chem. Phys.* **2015**, 17, 23859.
- [20] S. G. Haass, C. Andres, R. Figi, C. Schreiner, M. Bürki, Y. E. Romanyuk, A. N. Tiwari, *Adv. Energy Mater.* **2018**, 8, 1701760.
- [21] A. Mule, B. Vermang, M. Sylvester, G. Brammertz, S. Ranjbar, T. Schnabel, N. Gampa, M. Meuris, J. Poortmans, *Thin Solid Films* **2016**, 633, 156.
- [22] G. Altamura, M. Wang, K.-L. Choy, *Sci. Rep.* **2016**, 6, 22109.
- [23] J. Sangster, A. D. Pelton, *J. Phase Equilib.* **1997**, 18, 181.
- [24] L. L. C. Gaylord Chemical Company, DMSO solubility data, <http://www.gaylordchemical.com/literature/dmso-solubility-data> (accessed: February 2018).
- [25] J. C. A. Boeyens, F. H. Herbstein, *Inorg. Chem.* **1967**, 6, 1408.
- [26] J. R. Rumble, *CRC Handbook of Chemistry and Physics*, <http://hbcponline.com/faces/contents/ContentsSearch.xhtml> (accessed: February 2018).
- [27] G. Halleck, D. R. Cogley, J. N. Butler, *J. Electrochem. Soc.* **1969**, 116, 952.
- [28] T. Maeda, S. Nakamura, T. Wada, *Jpn. J. Appl. Phys.* **2011**, 50, 04DP07.
- [29] A. Nateprov, V. C. Kravtsov, G. Gurieva, S. Schorr, *Surf. Eng. Appl. Electron.* **2013**, 49, 423.
- [30] P. J. Dale, K. Hoenes, J. Scragg, S. Siebentritt, *Conf. Rec. IEEE Photovolt. Spec. Conf.*, Philadelphia, PA, June **2009**, p. 2080.
- [31] N. E. Brese, M. O'Keeffe, *Acta Crystallogr., Sect. B: Struct. Sci.* **1991**, 47, 192.
- [32] S. Chen, A. Walsh, X. G. Gong, S. H. Wei, *Adv. Mater.* **2013**, 25, 1522.
- [33] D. Shin, B. Saparov, D. B. Mitzi, *Adv. Energy Mater.* **2017**, 7, 1602366.
- [34] L. Choubrac, A. Lafond, C. Guillot-Deudon, Y. Moëlo, S. Jobic, *Inorg. Chem.* **2012**, 51, 3346.
- [35] L. Choubrac, M. Paris, A. Lafond, C. Guillot-Deudon, X. Rocquefelte, S. Jobic, *Phys. Chem. Chem. Phys.* **2013**, 15, 10722.
- [36] J. Márquez, M. Neuschitzer, M. Dimitrievska, R. Gunder, S. Haass, M. Werner, Y. E. Romanyuk, S. Schorr, N. M. Pearsall, I. Forbes, *Solar Energy Mater. Solar Cells* **2016**, 144, 579.
- [37] A. Weiland, J.-H. Zhang, D. J. Clark, J. A. Brant, C. W. Sinagra, Y. S. Kim, J. I. Jang, J. A. Aitken, *Dalton Trans.* **2017**, 46, 10102.
- [38] R. T. Ross, *J. Chem. Phys.* **1967**, 46, 4590.
- [39] W. Shockley, H. Queisser, *J. Appl. Phys.* **1961**, 32, 510.
- [40] F. Oliva, S. Kretzschmar, D. Colombara, S. Tombolato, C. M. Ruiz, A. Redinger, E. Saucedo, C. Broussillou, T. G. de Monsabert, T. Unold, P. J. Dale, V. Izquierdo-Roca, A. Pérez-Rodríguez, *Solar Energy Mater. Solar Cells* **2016**, 158, 168.
- [41] C. J. Hages, A. Redinger, S. Levchenko, H. Hempel, M. J. Koeper, R. Agrawal, D. Greiner, C. A. Kaufmann, T. Unold, *Adv. Energy Mater.* **2017**, 7, 1700167.
- [42] A. Redinger, S. Levchenko, C. J. Hages, D. Greiner, C. A. Kaufmann, T. Unold, *Appl. Phys. Lett.* **2017**, 110, 122104.
- [43] T. Unold, L. Gütay, *Adv. Charact. Tech. Thin Film Sol. Cells*, Wiley-VCH **2011**, pp. 151–175.
- [44] S. G. Haass, M. Diethelm, M. Werner, B. Bissig, Y. E. Romanyuk, A. N. Tiwari, *Adv. Energy Mater.* **2015**, 5, 1500712.
- [45] Y. T. Hsieh, Q. Han, C. Jiang, T. Bin Song, H. Chen, L. Meng, H. Zhou, Y. Yang, *Adv. Energy Mater.* **2016**, 6, 1502386.
- [46] A. Nagaoka, H. Miyake, T. Taniyama, K. Kakimoto, Y. Nose, M. A. Scarpulla, K. Yoshino, *Appl. Phys. Lett.* **2014**, 104, 152101.
- [47] M. A. Contreras, B. Egaas, P. Dippo, J. Webb, J. Granata, K. Ramanathan, S. Asher, A. Swartzlander, R. Noufi, in *Conf. Rec. IEEE Photovolt. Spec. Conf.*, Anaheim, CA, Marriott, September–October **1997**, p. 359.